Published by IOP Publishing for Sissa Medialab

Received: *February 10, 2026*
Accepted: *February 18, 2026*
Published: *March 18, 2026*

The pathfinder X-Ray axion telescope for the International Axion Observatory (IAXO) and axion searches at the CERN Axion Solar Telescope (CAST)

M.J. Pivovaroff,[a] **J. Ruz,**[a,b,*] **J.K. Vogel,**[a,b,*] **N. Brejnholt,**[a] **B. Budau,**[c] **V. Burwitz,**[c] **F.E. Christensen,**[d,e] **T. Decker,**[a] **C.J. Hailey,**[f] **R. Hill,**[a] **G. Hartner,**[c] **A. Jakobsen**[a,d] **and R. Soufli**[a]

[a] *Lawrence Livermore National Laboratory, Livermore 94550, CA, United States of America*
[b] *Fakultät für Physik. Technische Universität Dortmund. Dortmund, D-44221, Germany*
[c] *Max-Planck-Institut für extraterrestrische Physik, Garching D-85748, Germany*
[d] *National Space Institute, Technical University of Denmark, 2800 Kgs. Lyngby, Denmark*
[e] *Astrophysics and Atmospheric Physics, National Space Institute, Technical University of Denmark, 2800 Kgs. Lyngby Denmark*
[f] *Department of Astronomy and Astrophysics, Columbia University, New York 10027, United States of America*

E-mail: Jaime.Ruz@cern.ch, Julia.Vogel@cern.ch

Abstract: The axion, a hypothetical pseudo-scalar particle proposed by Peccei and Quinn to resolve the strong CP problem in quantum chromodynamics, remains one of the most compelling dark matter candidates. Axions and Axion-Like Particles (ALPs) are characterized by a broad and largely unconstrained parameter space in mass and coupling strength, motivating extensive experimental searches. The International Axion Observatory (IAXO) is a next-generation axion helioscope designed to achieve over an order of magnitude improvement in sensitivity to the axion-photon coupling constant $g_{a\gamma}$ relative to previous experiments such as the CERN Axion Solar Telescope (CAST). IAXO will employ large-scale superconducting magnets, precision x-ray optics, and ultra-low-background detectors to search for solar axions produced primarily via the Primakoff effect.

This work presents the design and performance of the IAXO pathfinder x-ray optic, a technological demonstrator that validated the optical concepts for IAXO through axion searches at CAST. Comprehensive ray-tracing simulations and experimental measurements were conducted to assess the optic's effective area, detection efficiency, and background suppression capabilities. Deployed at CAST in conjunction with Micromegas and GridPix detectors, the Pathfinder demonstrated record-setting sensitivity to both $g_{a\gamma}$ and the axion-electron coupling g_{ae}, establishing the most stringent laboratory constraints on solar axions to date. These results confirm the viability of the IAXO optical design and detector concept, providing a critical technological benchmark that informs the ongoing development of the BabyIAXO and full-scale IAXO telescopes.

Keywords: Imaging spectroscopy; Optics; X-ray detectors and telescopes; Particle detectors

*Corresponding author.

https://doi.org/10.1088/1748-0221/21/03/P03023

Contents

2026 JINST 21 P03023

1 Introduction

The axion is a hypothetical pseudo-scalar particle proposed by Peccei and Quinn [1, 2] to resolve the strong CP problem in quantum chromodynamics (QCD). Axions and related pseudo-scalars, collectively known as axion-like particles (ALPs) [3, 4], cover a wide range of possible masses and couplings, driving extensive global search efforts. Axions are also compelling dark matter candidates [5].

The International Axion Observatory (IAXO) [6] is a next-generation helioscope designed to extend the sensitivity of the CERN Axion Solar Telescope (CAST) [7, 8], which operated at CERN from 2003 to 2021 and set leading limits on the axion-photon coupling. IAXO, to be constructed at DESY (Hamburg), will employ a large magnetic volume, precision x-ray optics, and ultra-low-background detectors to search for solar axions [9].

IAXO aims to improve the sensitivity to the axion-photon coupling, $g_{a\gamma}$, by more than an order of magnitude, potentially reaching regions beyond current astrophysical bounds on the axion-electron coupling, g_{ae} [10]. Additional mechanisms, such as the M1 nuclear transition of ^{57}Fe at 14.4 keV, may also produce monoenergetic axions [11, 12].

This work presents the design and performance of the IAXO pathfinder x-ray optic, a technological demonstrator that validated the optical concepts for IAXO through axion searches at CAST. Deployed at CAST with Micromegas and GridPix detectors [13], the pathfinder demonstrated excellent focusing and background suppression, achieving record constraints on both $g_{a\gamma}$ [7, 8] and g_{ae} [14]. These results establish a solid experimental and technological foundation for BabyIAXO and the full IAXO experiment.

2 X-ray telescopes for axion helioscopes

To fully exploit the sensitivity of a strong, laboratory magnetic field for axion searches, axion helioscopes employ reflective x-ray focusing optics that resemble x-ray telescopes (XRTs). The x-ray optics concentrate or focus the essentially parallel photons, converted inside the magent bore, to a compact spot. This technique allows the use of small, low-background detectors — essential for achieving the ultra-low background levels required by BabyIAXO and IAXO. Beyond enhancing the signal-to-noise ratio, x-ray telescopes (XRTs) enable simultaneous signal and background measurements under identical conditions, with the focal region recording potential axion signals and the surrounding area serving as an in-situ background reference. The feasibility of this approach was first demonstrated by the X-ray telescope of CAST [15], which pioneered the use of x-ray focusing optics and established the experimental foundation for subsequent helioscope developments.

The performance of a XRT is characterized by three key, energy-dependent metrics: the size and shape of its point spread function (PSF); it's throughput, often called the effective area; and its field of view (FOV). These higher order properties, in turn, depend on the optical design and properties of the XRT, including the optical prescription, the focal legnth f, the lengths of the primary and second mirrors, and the coatings of the mirror surfaces. To achieve high reflectivity, XRTs usually employ substrates coated with gold or iridium that work at shallow grazing angles in the range of tenths to a few degrees. This operating principle employs pairs of full surface revolution mirrors, most commonly a paraboloid primary and a hyperboloid secondary. First proposed by Wolter [16], this design is similar to Cassegrain telescopes that operate in the visible and is commonly referred to as a Wolter I telescope. The Wolter I XRT offers the additional benefit that co-focal "shells" can be nested inside one another to achieve large effective areas. X-ray satellite missions like Einstein, ROSAT and Chandra demonstrated the power of XRTs, and the importance of this revolutionary technology was recognized by the broader scientific community when Riccardo Giacconi was awarded the 2002 Noble Prize in Physics for his pioneering research and leadership developing reflectivity x-ray telescopes.

The optics needed for CAST, BabyIAXO and IAXO benefit from two innovations pioneered by the x-ray astrophysics instrumentation community over the last decades. First, researchers have demonstrated several techniques to create sufficiently thin mirrors (with thicknesses typically in the range of tenths to a few millimeters) that can be highly nested. Techniques to create these mirrors include: replicating integral shells of nickel from mandrels, replicating aluminum foils from mandrels into mirror segments, and heating or "slumping" flat glass substrates into mirror segments. Second, the community has developed thin-film, multilayer coatings to allow XRTs to operate at larger graze angles and higher energies than achievable with monolithic coatings of gold or iridium. See Pivovaroff and Okajima [17] for a recent review of XRT designs and operating principles.

The CAST and IAXO collaboration has selected a cone-approximation Wolter I XRT design [18] because of their large throughput and favorable focusing properties in the 0.1−10 keV x-ray regime. The overall performance can be described by the figure of merit[1]

$$f_0 = \frac{\epsilon_0}{\sqrt{a}}, \tag{2.1}$$

where ϵ_0 is the throughput and a the focal spot area. Optimization involves balancing focal length, graze angle, and photon energy to match the solar axion spectrum and detector response.

[1]This figure of merit is not dimensionless, as there are additional terms that depend on the observing time, detector properties and magnet design.

2026 JINST 21 P03023

X-rays are primarily converted to axions in the Solar core (the innermost 0.1% volume) of the Sun and axion-transformed x-rays are emitted along the solar axion direction. The telescope FOV need only cover the inner three arcminutes (~ 0.9 mrad) of the solar disk, containing most of the flux. The differential solar axion flux is given by [19]

$$\frac{\mathrm{d}\phi_a}{\mathrm{d}E} = 6.02 \times 10^{10} g_{10}^2 E^{2.481} e^{-E/1.205} \ \mathrm{cm}^{-2}\mathrm{s}^{-1}\mathrm{keV}^{-1}, \tag{2.2}$$

where $g_{10} = g_{a\gamma}/(10^{-10}, \mathrm{GeV}^{-1})$ and E is in keV.

2.1 Multilayer mirror design

The two most powerful x-ray satellites, NASA's Chandra x-ray Observatory and ESA's XMM-Newton, utilize mirrors coated with a single high-density material: iridium for Chandra and gold for XMM-Newton. Although these coatings provide high reflectivity at photon energies up to about 10 keV, their performance declines sharply at higher energies. To overcome this limitation, multilayer coatings comprising alternating layers of high- and low-atomic-number (Z) materials have been developed.

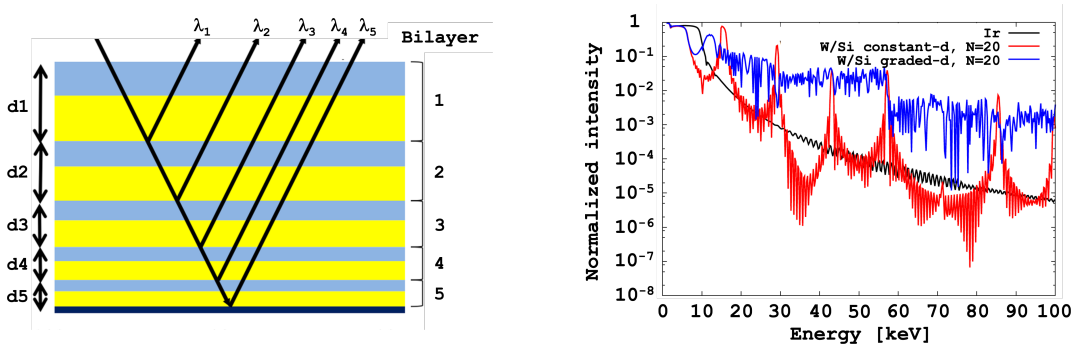

Figure 1. *Left*: Schematic of x-ray reflection in a depth-graded multilayer; thinner bilayers reflect higher-energy photons and thicker bilayers reflect lower-energy photons. *Right*: Simulated x-ray reflectivity as a function of photon energy at a grazing incidence angle of 0.5° for an Ir single layer (black), a W/Si constant-period multilayer (red), and a W/Si depth-graded multilayer (blue). The depth-graded multilayer provides high reflectivity over a broad energy range, exceeding the single layer configuration. Reproduced with permission from [20].

The periodic interfaces within these multilayers function as Bragg reflectors, thereby enhancing mirror reflectivity in the hard x-ray regime. Multilayers have been developed for a variety of applications — astrophysics [21], diagnostics for high energy density science facilities [22], nuclear safeguards [23] and preclincical nuclear medicine [24]–and proven to work well above 300 keV [25].

The main design parameters of a multilayer are the number of bilayers (N), the bilayer thickness (d), and the thickness ratio between materials (Γ). To achieve broad energy coverage, the d-spacing is often graded — linearly or by a power law [26], producing a smooth reflectivity curve suitable for focusing x-rays across a wide energy band. Interface quality strongly affects performance. The material pair (e.g., Pt/C or W/Si) must minimize roughness to preserve distinct Bragg reflections [27]. Figure 1 shows a schematic of a depth-graded multilayer and its reflectivity enhancement.

3 Pathfinder design and fabrication

Advances in reflective x-ray optics, particularly thermally-formed (or "slumped") glass substrates coated with multilayer coatings, led to the adoption of the techniques developed for the NASA

2026 JINST 21 P03023

NuSTAR mission [28] for CAST and IAXO. The optic was designed and assembled at Lawrence Livermore National Laboratory (LLNL, California, US). Researchers at the Technical University of Denmark (DTU, Copenhagen) designed and deposited multilayer coatings on flight-spare NuSTAR substrates. The slumped glass substrates were developed for NuSTAR by a collaboration led by Columbia University. Installation of the pathfinder XRT at the CERN Axion Solar Telescope was carried out in partnership with the University of Zaragoza (UNIZAR, Spain) [13]. After use for axion searches in CAST, the pathfinder optics was calibrated at the PANTER x-ray test facility of the Max Planck Institute for Extraterrestrial Physics (MPE, Germany).

3.1 Optics design

A key challenge in adapting NuSTAR glass optics for the CAST helioscope is the limited available space. The optic must be installed at the end of the magnet nearest the wall, leaving only about 2 meters to accommodate the optic, the detector, and the focal distance between them. Additionally, the small magnet bore diameter of 43 mm is smaller than the inner radius of the NuSTAR telescopes. These constraints are mitigated by the fact that the optic does not require a symmetric field of view and that the relevant axion spectrum is concentrated at relatively low energies. Figure 2 (left) shows a top-down view of the magnet bore, illustrating the placement of the optic and detector within the limited space.

To accommodate the narrow bore, the design uses only one-sixth of the azimuthal area of a typical circularly symmetric XRT: i.e., the optic has wedge shape similar to a generous slice of pie. Two mirror stacks are arranged to reflect x-rays toward one side. Each stack is tall enough to cover the magnet bore opening, while each mirror segment is sufficiently wide to ensure complete coverage. The NuSTAR mirror substrates, originally fabricated in 30 and 60° segments are well suited for this configuration. To minimize cost, surplus uncoated NuSTAR slumped-glass substrates were repurposed for the pathfinder optic.

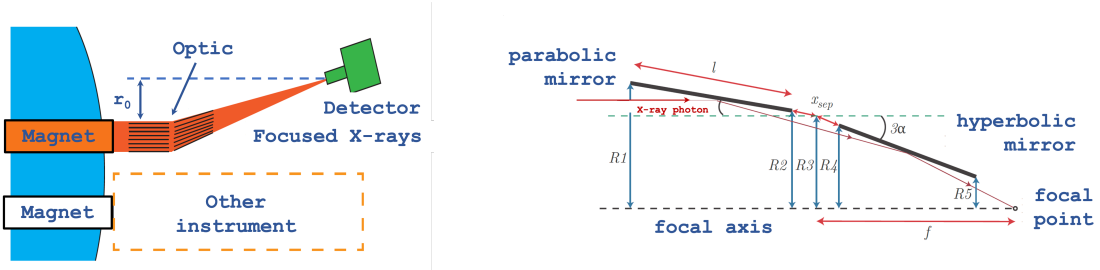

Figure 2. *Left*: Top-down view of the end of the CAST magnet, showing the placement of the pathfinder x-ray optic at one magnet bore. The second bore is occupied by another instrument, constraining the available space for the CAST XRT. *Right*: Diagram of a Wolter I telescope seen from the side with R1-R5 indicated. The principle of the Wolter I double reflection can be seen as an x-ray photon is reflected off the parabolic and hyperbolic mirrors. Here, l is the mirror length, f is focal length, x_{sep} is distance between parabolic and hyperbolic mirror and α is the angle of reflection for an x-ray photon parallel to the focal plane.

The optic design has a focal length of 1.5 m and a total of 13 nested mirror shell pairs to fully illuminate the 43 mm CAST magnet bore which achieves complete bore coverage while maintaining the necessary focusing performance within the tight space constraints of the CAST facility. The

2026 JINST 21 P03023

Table 1. Layer parameters for pathfinder optics. Based on the geometry within circle given in figure 3 (left).

Layer	Area [mm^2]	α [°]	α [mrad]	R1 [mm]	R5 [mm]
1	13.863	0.579	10.113	63.006	53.821
2	48.175	0.603	10.530	65.606	56.043
3	69.270	0.628	10.962	68.305	58.348
4	86.760	0.654	11.411	71.105	60.741
5	102.266	0.680	11.877	74.011	63.223
6	116.172	0.708	12.360	77.027	65.800
7	128.419	0.737	12.861	80.157	68.474
8	138.664	0.767	13.382	83.405	71.249
9	146.281	0.798	13.921	86.775	74.129
10	150.267	0.830	14.481	90.272	77.117
11	149.002	0.863	15.062	93.902	80.218
12	139.621	0.898	15.665	97.668	83.436
13	115.793	0.933	16.290	101.576	86.776

geometry of the optic follows the standard cone-approximation Wolter-I prescription, defined by

$$\tan(4\alpha) = \frac{R_3}{f}, \tag{3.1}$$

where α is the grazing-incidence angle, f is the focal length, and R_3 denotes the radius between the optical axis and the midpoint between the parabolic and hyperbolic mirror surfaces. A schematic of the relevant design parameters is shown in figure 2 (right). To align the telescope with the CAST magnet bore, an offset r_0 between the bore and the telescope focal axis is introduced.

The NuSTAR mirror segments have a length l of 225 mm, a dimension retained in our pathfinder configuration to ensure substrate compatibility and maintain optimal focusing performance. Additional geometric parameters are defined as follows: x_{sep} is the separation between the parabolic and hyperbolic mirrors; R_1 and R_2 represent the radii from the optical axis to the front and back of the first mirror stack, respectively; and R_4 and R_5 correspond to the front and back of the second mirror stack. The complete optical layout is illustrated in figure 3, while the calculated radii and incidence angles for each layer are summarized in table 1.

3.1.1 Optimization of the reflective coatings

To maximize the optical efficiency, the mirror coatings were optimized for the relevant x-ray energy regime (see eq. (2)). Unlike conventional astrophysical observatories, which must accommodate broad and diverse spectra, the pathfinder telescope observes a single, well-defined source with a narrowly constrained spectral distribution. This allows the coating design to be specifically tailored for maximum reflectivity within that energy band. The detector's quantum efficiency is also well characterized, enabling a comprehensive optimization of the overall system performance.

The mirrors are implemented as conical approximations of a Wolter-I geometry, with grazing incidence angles ranging from 0.579° for the innermost shell to 0.933° for the outermost shell. For this configuration, the optimal coating parameters were determined by maximizing a figure of merit

2026 JINST 21 P03023

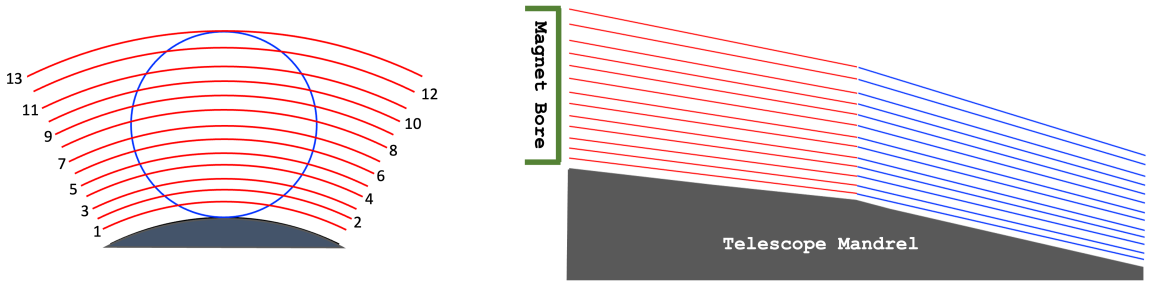

Figure 3. On the left, illustration of magnetic bore (blue) and the 13 optics layers (red) covering the bore opening. On the right, a 1:3 scale side-view of primary (red) and secondary (blue) mirrors.

(FOM) that quantifies the combined performance of the pathfinder and detector subsystems:

$$\mathrm{FOM} = \int_{0.1}^{10} R^2(\alpha, E)\, Q_{\mathrm{det}}(E)\, \phi_{\mathrm{a}}(E)\, dE, \tag{3.2}$$

where $R^2(\alpha, E)$ represents the squared reflectivity accounting for the two reflections within the telescope, $Q_{\mathrm{det}}(E)$ is the detector quantum efficiency, and $\phi_{\mathrm{a}}(E)$ denotes the solar axion spectrum.

Multilayer coatings based on W/B4C, W/Si, Pt/C, Pt/B4C, and Ni/B4C, as well as single-layer coatings of W, Pt, Ir, and Ni, were evaluated. Each material combination was optimized according to eq. (3.2) with surface and interface roughness fixed at 0.5 nm; consistent with previous NuSTAR designs. Both linearly graded and constant-d multilayers were modeled.

Following the optimization process, coatings based on boron carbide exhibited a slightly higher figure of merit; however, they were excluded from consideration due to concerns regarding their long-term stability [29]. Platinum-carbon (Pt/C) multilayers were therefore selected as the baseline coating material: layers 1–3 (Recipe.1), layers 4–7 (Recipe.2), layers 8–11 (Recipe.3), and layers 12–14 (Recipe.4) [20]. Figure 4 shows a table for the layout of each multilayer recipe used for the pathfinder x-ray optic (right) and the performance of each recipe in comparison to the Primakoff axion spectra arriving from the Sun (right).

3.2 Multilayer coating and characterization at DTU Space and LBNL/ALS

The pathfinder x-ray telescope employed repurposed Schott D263 borosilicate glass substrates, originally produced for the NuSTAR mission meeting the surface roughness requirement of less than 0.5 nm. Thermally molded substrates with curvatures best matching the specified diameters for the 13 mirror layers were selected from surplus stock [20]. The four optimized Pt/C coating recipes were prepared for the pathfinder x-ray optic, covering a total of 56 substrates with 12–16 pieces per recipe. Each sample was characterized at two experimental facilities. Measurements at the DTU x-ray Facility were performed at a fixed photon energy of 8.048 keV while varying the incidence angle. Complementary measurements were carried out at the Advanced Light Source (ALS) at Lawrence Berkeley National Laboratory (LBNL), a third-generation synchrotron source, over an energy range of 0.05–1.2 keV. At ALS, data were collected at fixed incidence angles of 5° and 8°, while scanning the photon energy.

The measured x-ray reflectivity (XRR) data were fitted using the IMD modeling software [30, 31]. Figure 5 shows the comparison between the experimental data and the corresponding IMD models.

2026 JINST 21 P03023

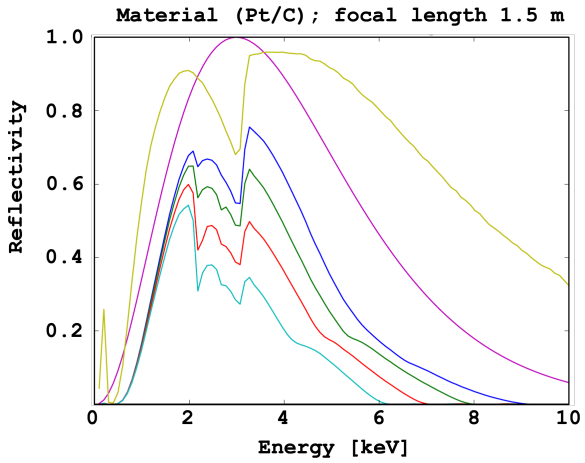

	Layer	Bilayers	d_{min}	d_{max}	Γ
	1	2 (R.1)	11.5	22.5	0.45
	4	3 (R.2)	7.0	19.0	0.45
	8	4 (R.3)	5.5	16.0	0.4
	12	5 (R.4)	5.0	14.0	0.4
	Axion spectrum				
	Detector quantum efficiency				

Figure 4. *Left*: Simulation of the figure of merit for the selected multilayer coatings applied to the pathfinder x-ray optic. The four optimized coating recipes correspond to mirror layers 1–3, 4–7, 8–11, and 12–14. The computed performance includes the detector's quantum efficiency. *Right*: Recipe descriptions of pathfinder x-ray mirrors.

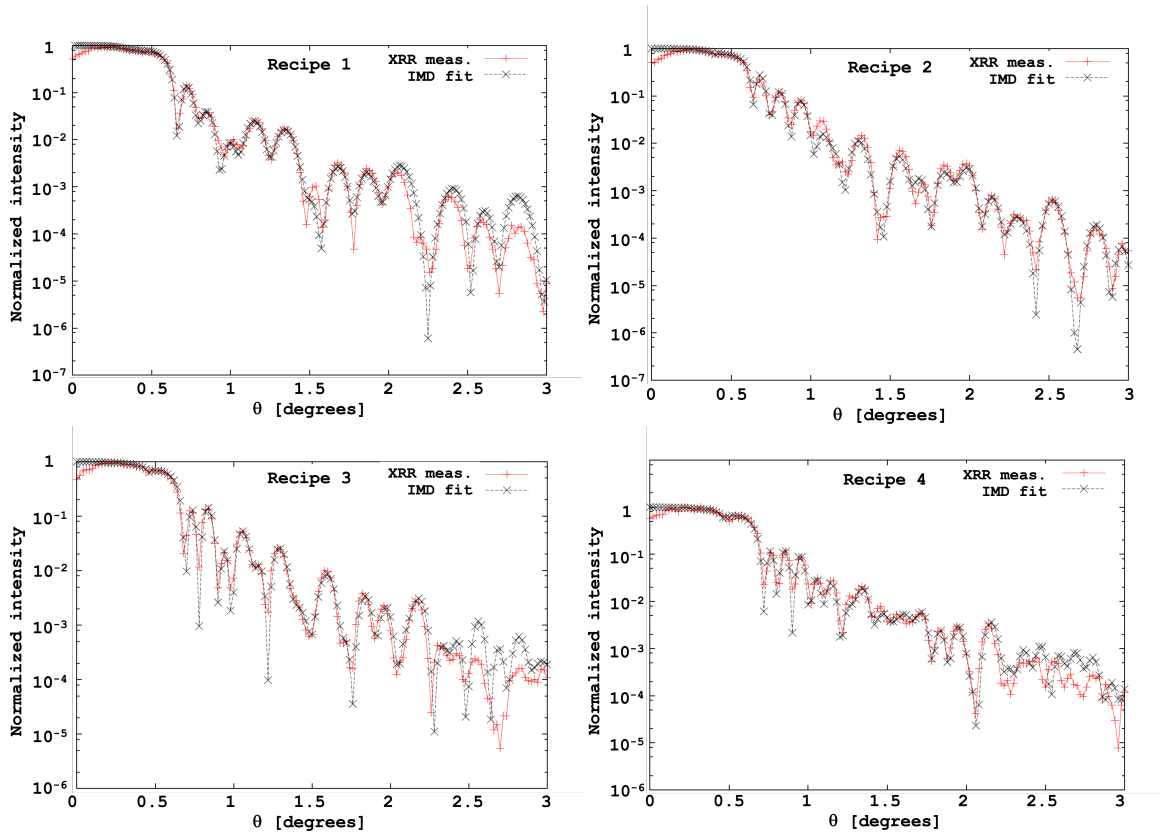

Figure 5. XRR measurement of witness samples from pathfinder mirror recipes 1 to 4 coating (red) in comparison to IMD model fits (black). Measurements where performed at 8.048 keV.

Despite the complexity of modeling graded-d coatings, where each layer thickness and interface roughness is treated as an independent variable, the fits show good agreement with the measurements,

2026 JINST 21 P03023

obtaining interface roughness values for Pt/C and C/Pt layers in the range of approximately 0.25–0.35 nm. Further characterization of the multilayer structure revealed that the platinum (Pt) layers are chemically pure but exhibit a slightly reduced density of 20.2 g/cm^3, compared to the bulk value of 21.45 g/cm^3. In contrast, the carbon (C) layers are not chemically pure, exhibiting a measured stoichiometry of approximately 95.8% C, 2.3% Fe, 1.3% Ar, and 0.6% Cr, and a density of 2.1 g/cm^3. Nevertheless, the measured reflectivity performance of the sampled multilayer recipes agrees well with the design expectations and simulated specifications.

3.3 Assembly of the pathfinder optic

The pathfinder optic assembly was conducted at Lawrence Livermore National Laboratory using a NuSTAR-type assembly machine configured to fabricate a 30° azimuthal sector of the substrate array. A custom titanium mandrel was employed as the reference surface to ensure accurate alignment. Three graphite spacers were initially bonded to the mandrel using a precision epoxy and subsequently machined to achieve the targeted thickness and angular slope corresponding to the first-layer substrates of the first and second mirror stages, thereby establishing the base reference for the optic stack.

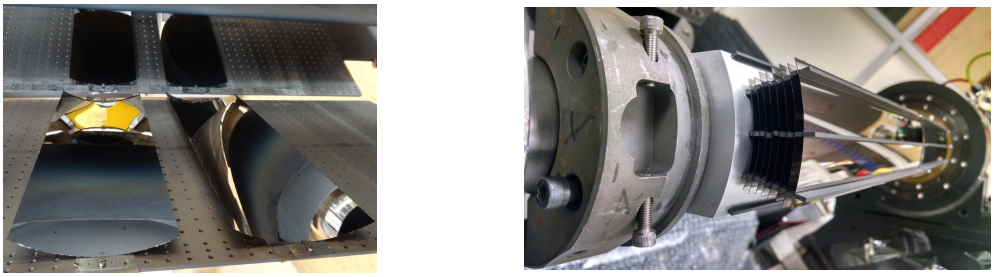

Figure 6. *Left*: Substrates in the coating chamber. *Right*: Glass substrates on the Titanium mandrel during assembly, with graphite spacers machined to thickness before stacking the next substrate.

The first-layer substrates were then positioned and mounted onto the machined spacers. Successive layers were constructed by bonding additional graphite spacers atop the preceding substrate layer, each spacer being machined in situ to the specified thickness to maintain the designed focal geometry and optical alignment (see figure 6).

The overall assembly approach closely followed the established procedures developed for the NuSTAR x-ray telescopes [32]. Minor modifications were implemented to accommodate the specific geometry and material properties of the pathfinder design, including adjustments to the mandrel configuration and spacer machining tolerances to optimize layer uniformity and minimize cumulative alignment errors.

4 Pathfinder optics response

4.1 Ray-trace modeling

To evaluate the theoretical throughput of the pathfinder optic, a dedicated ray-tracing simulation code was developed based on IDL routines [33]. The code models the optical response as a function of the x-ray source properties, including its distance, spatial extent (point-like or extended), and its position relative to the optical axis (on-axis or off-axis).

2026 JINST 21 P03023

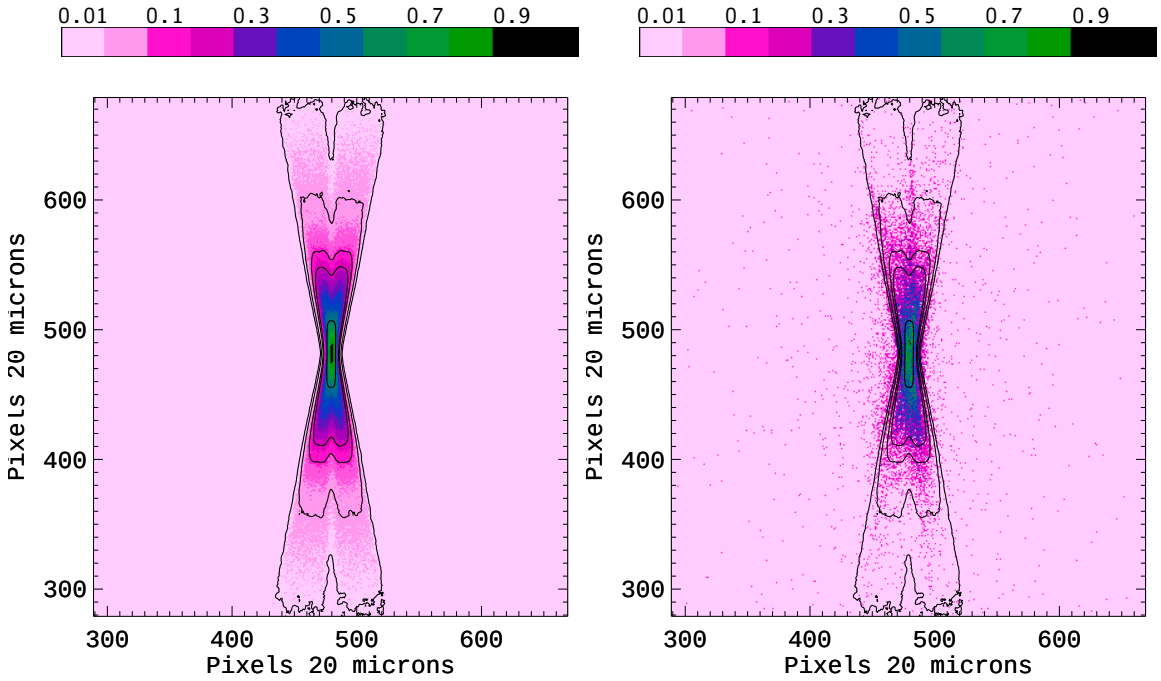

Figure 7. *Left*: Simulation of raw HPD at focal length of 1519 mm. Contour values of simulation are shown by the solid bold black lines at 2, 5, 10, 20, 50 and 80% of maximum intensity. *Right*: Cumulative data obtained at PANTER for raw HPD at focal length of 1519 mm. Contour values of simulation are also shown by the solid bold black lines at 2, 5, 10, 20, 50 and 80% of maximum intensity for comparison.

As a first step in the optical performance evaluation, a detailed ray-tracing simulation was conducted to characterize the pathfinder's point spread function and to estimate the precise location of the focal plane. The simulation modeled photon trajectories through the multilayer-coated mirror shells, accounting for surface figure errors, roughness, and alignment tolerances. By analyzing the spatial distribution of photon impacts at varying distances along the optical axis, the focal plane position corresponding to the minimum PSF width was determined. Figure 7 presents a comparison between the simulated image at the pathfinder's focal plane (left) and the measured point-spread distribution (PSD) for aluminum K_α x-ray photons (right). The ray-tracing simulation not only provides a quantitative assessment of the optic's imaging quality but also identifies the optimized focal distance for detector placement. In addition, the resulting PSF served as a benchmark for subsequent throughput and effective-area studies, as well as for comparison with experimental monitoring runs obtained during the pathfinder's deployment at CAST.

4.2 Characterization at the PANTER X-Ray test facility

The pathfinder x-ray optic was calibrated at the PANTER x-ray test facility of the Max Planck Institute for Extraterrestrial Physics (MPE). The calibration campaign consisted of a series of coordinated measurements designed to accurately characterize the optic's performance. The optic under test was mounted within the beamline under vacuum conditions to minimize x-ray absorption and scattering by air. A well-characterized x-ray source with selectable energies was positioned $\sim$ 130 m from the optic to provide a stable and collimated beam. Precise alignment of the optic was achieved using motorized XYZ translation stages, while the pitch and yaw were optimized to maximize photon throughput. Prior to each measure-

2026 JINST 21 P03023

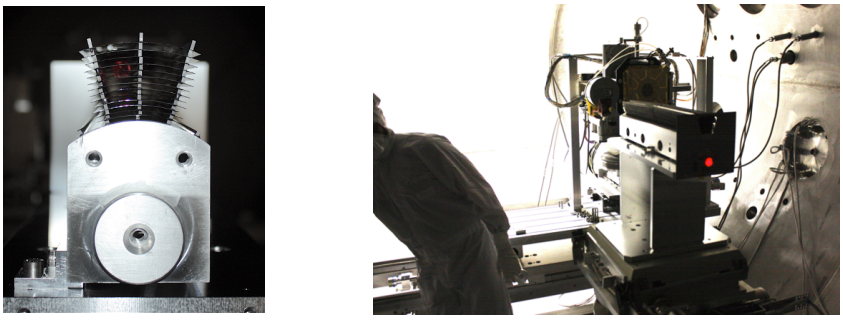

Figure 8. *Left*: Picture of the pathfinder x-ray optic previous to its calibration at the PANTER facility.*Right*: Image of the pathfinder inside the PANTER vacuum chamber during its preliminary alignment with the calibrated laser.

ment, the incident beam was characterized using reference detectors and monitoring instruments to determine its intensity, divergence, and energy spectrum. This ensured that the x-ray flux and beam profile were well defined for quantitative calibration. The optic focused the incident beam onto the TROPIC imaging detector [34]. See figure 8 for images of the pathfinder within the vacuum chamber of the PANTER facility.

By scanning the detector along the focal axis and recording the x-ray intensity distribution, the spatial resolution, focal length, and PSF of the pathfinder optic were accurately determined. The Effective Area of the pathfinder optic was determined by comparing the reflected x-ray flux to the incident flux, accounting for the TROPIC detector efficiency. This procedure enables calibration of the optic's throughput as a function of photon energy and grazing incidence angle. Measured parameters including the focal spot size, PSF, and Effective Area were subsequently compared with theoretical predictions derived from our ray-tracing simulations and optical models.

Comprehensive intra-focal, extra-focal, and at focus measurements were conducted to study the optic's imaging behavior and to identify figure errors arising from individual mirror shells. Intra-focal and extra-focal measurements were performed at positions 25 cm in front of and 20 cm behind the focal plane. In the following sections we present a detailed comparison between the results obtained during the pathfinder calibration at the PANTER facility and the expected performance from our simulations.

4.2.1 Point spread function and in-focus characterization

The pathfinder optic was designed for a nominal focal length of $f = 1500\,\text{mm}$, assuming a point-like source located at infinity. During characterization at the PANTER facility, however, the finite source-to-optic distance required a correction to the focal position. For a source distance of $D = 130.297\,\text{m}$, the image distance can be estimated from

$$\frac{1}{f}_{\text{eff}} = \frac{1}{f} - \frac{1}{D}, \tag{4.1}$$

which yields $f_{\text{eff}} \approx 1517\,\text{mm}$, i.e., a focal shift of approximately 17 mm beyond the nominal design value. Ray-tracing simulations that account for both the finite source distance and the extended nature of the PANTER beam predicted a focal position of 1519 mm (see figure 9). Remarkably, our simulations closely matched the empirical measurement of the pathfinder's focal length obtained at PANTER, showing only a 0.02% deviation from the actual data, that determined the focal position for the Al K_α line at 1519.4 mm. This excellent agreement confirms the accuracy and predictive reliability of the pathfinder ray-tracing model.

2026 JINST 21 P03023

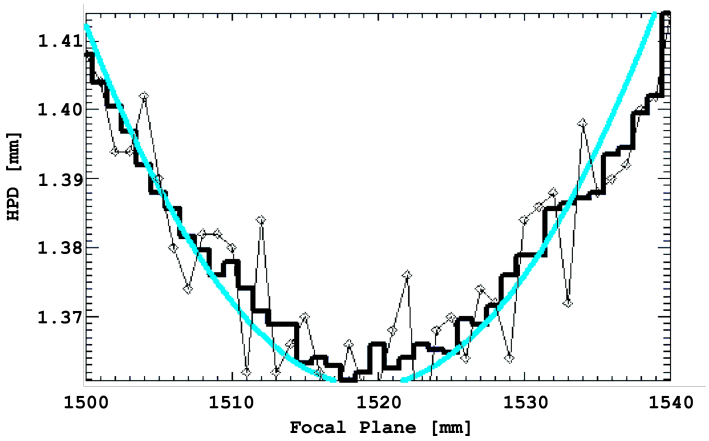

Figure 9. Simulated focal length for the PANTER setup.

Figure 10 illustrates the performance of the pathfinder x-ray optic for three of the nine characteristic x-ray energies measured at PANTER. In particular, the top row shows, from left to right, focal-plane scatter plots for Al K_α, Ti K_α, and Fe K_α measurements, together with contours at 1, 10, 50, 80, and 90% of the peak intensity from ray-tracing simulations. The bottom row presents cumulative intensity profiles along the horizontal (blue) and vertical (red) axis, with simulated profiles shown as dashed lines. The point spread function exhibits a clear energy dependence, with the encircled energy function narrowing at higher energies. This arises from the reduced contribution of the outermost mirror shells, which have lower reflectivity and larger optical aberrations, resulting in an overall PSF narrowing (see figure 11). Table 2 summarizes half-power diameter enclosing 50% of the total energy, as well as 80% and 90% for the Al, Ti, and Fe K_α lines at energies of 1.49, 4.51 and 6.4 keV respectively. Values obtained from our PANTER experimental measurements are compared to the ray-trace simulations. The observed imaging performance is well explained by mirror figure errors and design-induced aberrations, with excellent agreement between simulation and measured performance.

The primary factors determining the point spread function of our pathfinder are the figure errors of the mirror substrates and any optical aberrations inherent to the telescope design. To first order, these contributions can be treated as uncorrelated, allowing the total half-power diameter (HPD) to be approximated as

$$\mathrm{HPD}_{\mathrm{Total}} = \sqrt{\mathrm{HPD}^2_{\mathrm{figure}} + \mathrm{HPD}^2_{\mathrm{design}}}. \tag{4.2}$$

Table 2. Combined table with grouped datasets for HPD measurements at PANTER.

		50% HPD		80%		90%	
		[arcsec]	[mm]	[arcsec]	[mm]	[arcsec]	[mm]
Al K_α	PANTER data	207	1.52	397	2.92	549	4.04
	PANTER ray-trace	212	1.56	391	2.88	559	4.12
Ti K_α	PANTER data	196	1.44	380	2.80	511	3.76
	PANTER ray-trace	206	1.52	380	2.80	559	4.12
Fe K_α	PANTER data	196	1.44	364	2.68	483	3.56
	PANTER ray-trace	185	1.36	348	2.56	516	3.80

2026 JINST 21 P03023

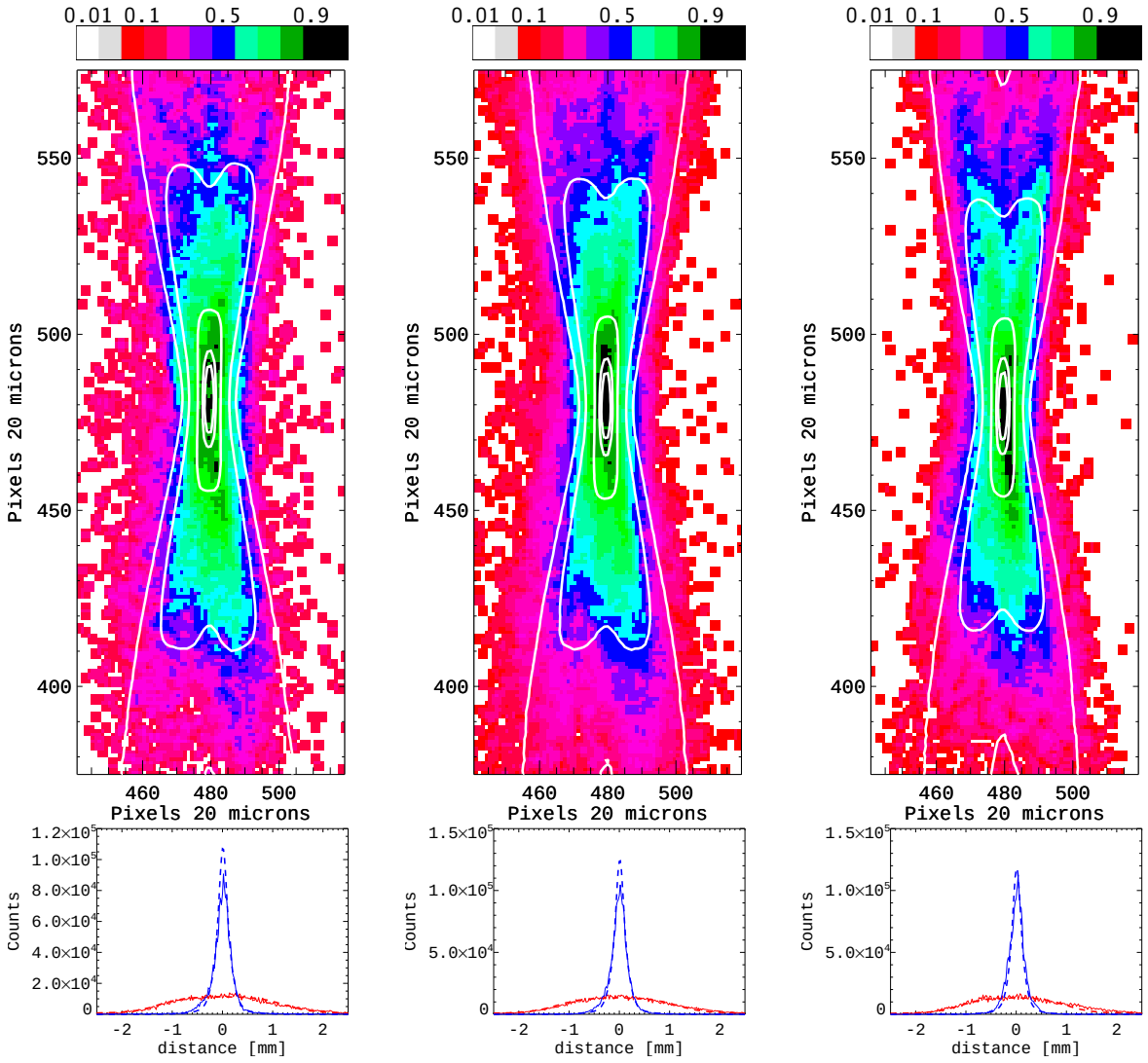

Figure 10. *Top*: Measured scatter plots at focus for Aluminum (left), Titanium (center) and Iron (right) K_α energies at the PANTER facility. Overlapped, in yellow, expected contour levels at 1, 10, 50, 80 and 90%. *Bottom*: Cumulative plots along the horizontal (blue) and vertical (red) axis for Aluminum (left), Titanium (center) and Iron K_α (right) energies.

For x-ray telescopes intended for general-purpose astrophysics, performance is traditionally dominated by mirror figure errors. In a true Wolter I design (e.g., ABRIXAS), on-axis optical aberrations are negligible, and image quality is set primarily by the accuracy of the mirror surfaces. In contrast, cone-approximation Wolter I designs, as used in NuSTAR and our pathfinder x-ray telescope, inherently introduce design-induced optical aberrations. For example, NuSTAR's design corresponds to an idealized $\mathrm{HPD}_{\mathrm{design}}$ of 7″. However, the measured on-orbit $\mathrm{HPD}_{\mathrm{total}}$ is 58″, indicating that its performance is overwhelmingly dominated by mirror figure errors, yielding $\mathrm{HPD}_{\mathrm{figure}} \approx 57''$. Our ray-tracing simulations for the pathfinder indicate that the design-induced optical aberration ($\mathrm{HPD}_{\mathrm{design}}$) exceeds 120″. This arises from the relatively large mirror length (225 mm) in comparison to the focal length (1500 mm), which produces substantial geometric aberrations. As a result, the pathfinder optical design would be suboptimal for conventional astronomical imaging. However, the pathfinder optic

2026 JINST 21 P03023

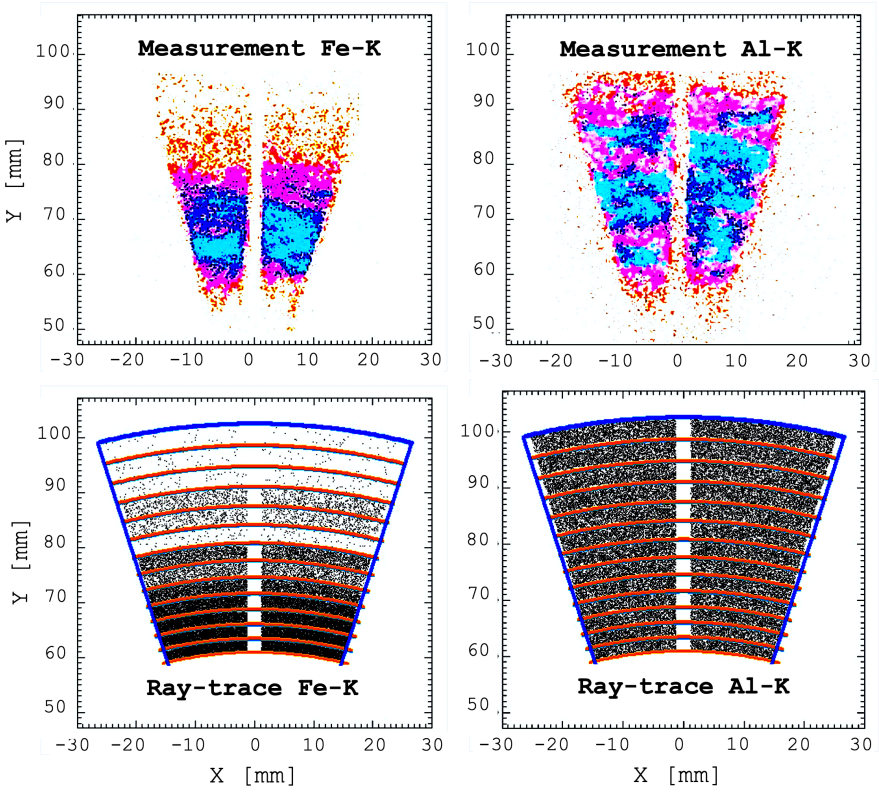

Figure 11. *Top*: Intra-focal measurements of Iron K_α (left) and Aluminum K_α (right). *Bottom*: Ray-tracing simulation of the telescope optic, showing an end-on view looking directly into the entrance aperture. Each balck dot represents an individual photon. The blue and red curves denote the outer pathfinder mask and the edges of each mirror shell, respectively. Photons that successfully reflect from the paraboloid (upper) and hyperboloid (lower) surfaces are back-projected to illustrate the optical geometry. The vertical stripe, corresponding to a region lacking photon counts, arises from the series of graphite spacers separating adjacent shells. In the ray-tracing model, the spacer width is adjusted to match the PANTER measurement data. The physical spacer width is 1.6 mm, with an additional effective width of approximately 0.6 mm attributed to epoxy "squeeze-out" ($\sim$ 0.3 mm on each side).

was specifically designed to image the central three-arcminute (180″) region of the solar disc. Within this limited field of view, the level of optical aberration remains acceptable for its intended purpose.

4.2.2 Effective area

A fundamental performance metric for telescopes across the optical, UV, and x-ray regimes is the effective area, which measures the telescope's photon-collecting capability at each wavelength or energy E. It is obtained by multiplying the telescope's reflecting area by the normalized reflectivity spectrum, though the calculation is not simple, since there exist an angular dependence for reflectivity.

In x-ray telescopes with concentric mirror shells, each shell reflects photons at a different angle θ_i, yielding a distinct reflectivity spectrum. Wolter I optics require double reflections, so the reflectivity is squared. The effective area of the telescope is calculated by combining the contributions from all individual shells, where $R_i(E, \theta_i)$ is the reflectivity of an individual cell at the relevant incident angle

2026 JINST 21 P03023

Table 3. Measured effective area and associated uncertainties for various x-ray fluorescence lines.

Line	Energy [keV]	Effective Area [cm^2]	Stat. Error [cm^2]	Sys. Error [cm^2]
C Kα	0.277	8.29	±0.08	±0.20
Cu Lα	0.93	7.64	±0.08	±0.20
Al Kα	1.486	8.32	±0.05	±0.20
W Mα	1.775	8.38	±0.08	±0.20
Ag Lα	2.98	5.16	±0.05	±0.10
Ti Kα	4.51	3.12	±0.01	±0.08
Cr Kα	5.41	2.54	±0.02	±0.06
Fe Kα	6.40	1.18	±0.01	±0.03
Cu Kα	8.04	0.154	±0.001	±0.004

and A_i is the shell's cross-sectional area. For a telescope with N shells, the total effective area is

$$A_{\text{eff}} = \sum_{i=1}^{N} A_{\text{eff},i}(\theta_i) = \sum_{i=1}^{N} R_i^2(E, \theta_i)\, A_i \tag{4.3}$$

Maximizing the effective area is essential for detecting the faint flux of soft and hard x-rays from distant sources. Once the optical geometry is established, the mirror coatings must be carefully optimized, considering material choice, coating thickness, number of bilayers, and shell-to-shell variations to achieve maximum throughput. This study has already been detailed in section 3.1.

At PANTER, the effective area of the pathfinder was experimentally determined using three sequential exposures: a direct x-ray beam (I_0), the beam reflected by the optic under test, and a subsequent direct beam measurement. Event lists were reprocessed with energy thresholds optimized to maximize counts in the primary spectral peak. Poisson errors were derived from counting statistics, and systematic uncertainties were estimated at ±2.5%. The telescope effective area was measured at nine distinct x-ray energies (see table 3).

We compared the experimental measurements at PANTER with ray-trace simulations using optical constants obtained for each witness sample in separate campaigns at the Advanced Light Source (ALS) and the DTU x-ray facility. Both datasets are in close agreement and accurately reproduce the PANTER measurements above 2 keV. However, the model based on the 8 keV DTU dataset systematically overestimates the effective area between 0.5 and 2 keV, which is consistent with the absence of trace high-Z contaminants that could reduce mirror reflectivity. Our ALS-derived models, based on measurements between 0.05 and 1.2 keV, incorporate the effects of such contaminants at low-energies and provide a more accurate representation of the telescope's effective area.

Extensive epoxy studies conducted during NuSTAR telescope development indicate that trace hydrocarbon residues are likely present on the optics. To assess the potential impact of a hydrocarbon film in the pathfinder, we modeled an absorbing layer of poly(methyl methacrylate) (PMMA) with a density of 1.38 g/cm^3 and stoichiometry $C_5H_8O_2$. Even extremely thin layers, on the order of 4–8 Å, can significantly affect the effective area. Based on visual inspection of the modeled curves, rather than formal fitting, we adopt a baseline assumption of an 8.0 Å PMMA layer on the telescope coatings to account for this contamination. These multilayer recipes were used to compute the telescope

2026 JINST 21 P03023

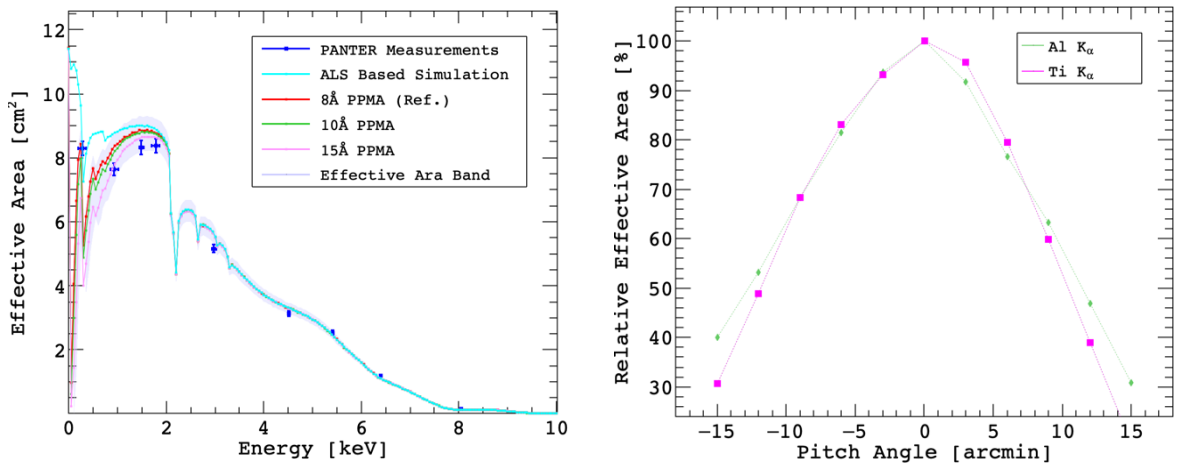

Figure 12. *Left*: Measured effective area and statistic uncertainties (dark blue points). In cyan, ray-trace simulation estimate for the PANTER data. Also, effective area estimates for superficial PMMA contamination of 8 Å (red), 10 Å (green) and 15 Å (pink). In gray, effective area upper and lower model band. **Right:** Off-axis response of the pathfinder x-ray optic for Aluminum K_α (light green) and Titanum K_α (pink).

effective area for solar axion measurements. To establish systematic bounds, simulations were first performed without any absorbing layer, and the resulting effective area was uniformly increased by 5% to define an upper bound. Conversely, a 8.0 Å absorbing layer was included in simulations, followed by a uniform 5% reduction in effective area, to define a lower bound. These upper and lower bounds quantify the systematic uncertainty in our effective area calculations. Contamination impacts are noticeable only at soft x-ray energies (E < 2 keV). The absolute value of the effective area at any given energy does not affect the 2D probability distributions, as our point-spread function model is purely geometric and contains no energy-dependent scattering terms. See figure 12 (left).

Fine alignment of the pathfinder x-ray telescope was performed to maximize the fluency of Aluminum K_α photons by adjusting both pitch and yaw angles. The pitch corresponds to rotation around the y-axis (parallel to the optical axis), while the yaw corresponds to rotation around the z-axis (orthogonal to the optical axis). During the alignment, the x-ray beam incidence was fixed along the x-axis, ensuring that variations in detected flux could be directly attributed to changes in the telescope orientation. This procedure allowed precise optimization of the telescope pointing to achieve maximum photon throughput. Vignetting analysis was also performed with Aluminum and Titanium K_α x-rays. Figure 12 (right) illustrates the pathfinder behavior as a function of angular orientation.

Effective area measurements at PANTER were performed extra-focally (see figure 13), positioning the detector 20 cm away from the telescope's nominal focal plane. This configuration minimizes pile-up in the detector, that could otherwise bias the measured count rates and reduce the accuracy of the effective area determination. By operating extra-focally, the photon flux is spread over a larger detector area, ensuring that counting statistics more accurately reflect the telescope's true collecting efficiency.

5 Axion analysis and results

Because the telescope's throughput and point spread function depend strongly on both photon energy and graze angle, our design studies incorporate the expected solar axion energy spectrum (eq. (2)) and the field of view of axion-induced x-rays, which are emitted along the direction of the incoming

2026 JINST 21 P03023

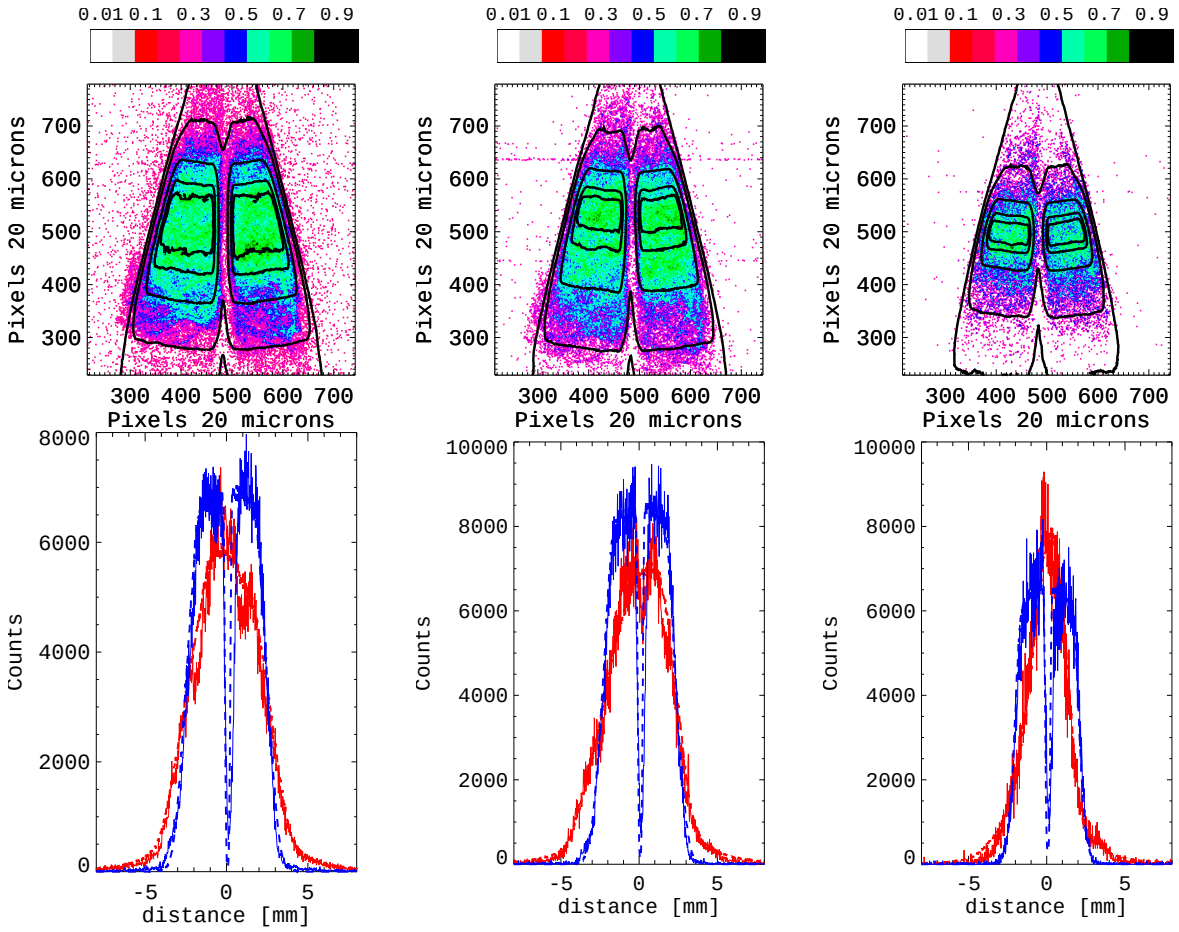

Figure 13. *Top*: From left to right, scatter plots at extra-focal distance for Aluminum (left), Titanium (center) and Iron K_α (right) energies at the PANTER facility. Overlapped, in black, expected contour levels at 1, 10, 50, 80 and 90% of maximum intensity from the ray-trace simulation code. *Bottom*: From left to right, cumulative plots along the horizontal (blue) and vertical (red) axis for the Aluminum (left), Titanium (center) and Iron K_α (right). Overlapped, in dashed blue and dashed red, expected signal from ray-trace simulation code.

solar axions. Consequently, the telescope's FOV only needs to cover slightly more than the inner three arcminutes (0.9 mrad) of the solar disk, where the majority of axion production occurs. Most of the Primakoff axion flux is confined within approximately $0.2\,R_\odot$. This optimization strategy guided the design of the pathfinder telescope to maximize experimental sensitivity when operated at the CAST experiment.

To ensure the correct implementation of the pathfinder at CAST, a detailed alignment of the optic and detector was carried out with the assistance of CERN geometers. Additionally, a COOL-X x-ray source was positioned on-axis, 14.2 m from the optic on the opposite side of the magnet bore, to monitor the relative XY position and tilt of the focal spot within the Micromegas detector coordinate system [13]. The detector, pathfinder, and COOL-X were subsequently integrated into the vacuum beamline of the CAST magnet in preparation for the upcoming data-taking campaigns. The pathfinder successfully reflected the 6 mm-diameter beam from the COOL-X source, which produced photons in the 0–10 keV energy range. Ray-tracing simulations reproducing the in-situ geometry of the COOL-X setup at CAST yielded a half-power area (HPA) of 8.6 mm^2 for this configuration. As illustrated in

figure 14, the simulated datasets show excellent agreement with the detector measurements, confirming the accuracy of the IDL-based ray-tracing model. Together, the experimental data and simulation routines determined a relative tilt of $-5.2°$ with respect to the x-axis of the Micromegas detector plane.

The first stage of our axion analysis includes a calculation of both the total Primakoff axion flux available at CAST and the actual throughput of the Pathfinder telescope, incorporating the effective area measured at PANTER. This study also accounts for the telescope alignment accuracy relative to the incident photon direction, which at CAST is within the geometric tolerance of 250 μm over a 10 meter optical path (equivalent to 0.09 arcmin). From figure 12 (right panel), it can be seen that this alignment precision is nearly four times better than the vignetting tolerance measured at PANTER, ensuring at least 99% of the available throughput from the Pathfinder. This holds for both aluminum and titanium K_α energies, which require alignment within ±0.4 arcmin to preserve 99% of the effective area.

Complementary simulations were performed to model the CAST cold-bore configuration during solar tracking, where solar axions are expected to convert into x-rays within the magnetic field. For a 3′-diameter extended source and an optic figure error of 1′, comparable to that of the NuSTAR telescope, the modeled point-spread function, shown in figure 7, produced an HPA of 1.44 mm^2, which is close to a perfect optic with zero figure error where the HPA decreases slightly to 1.39 mm^2. These results demonstrate that the pathfinder x-ray telescope performs close to its theoretical limit, and confirm the high optical precision achieved in the pathfinder design.

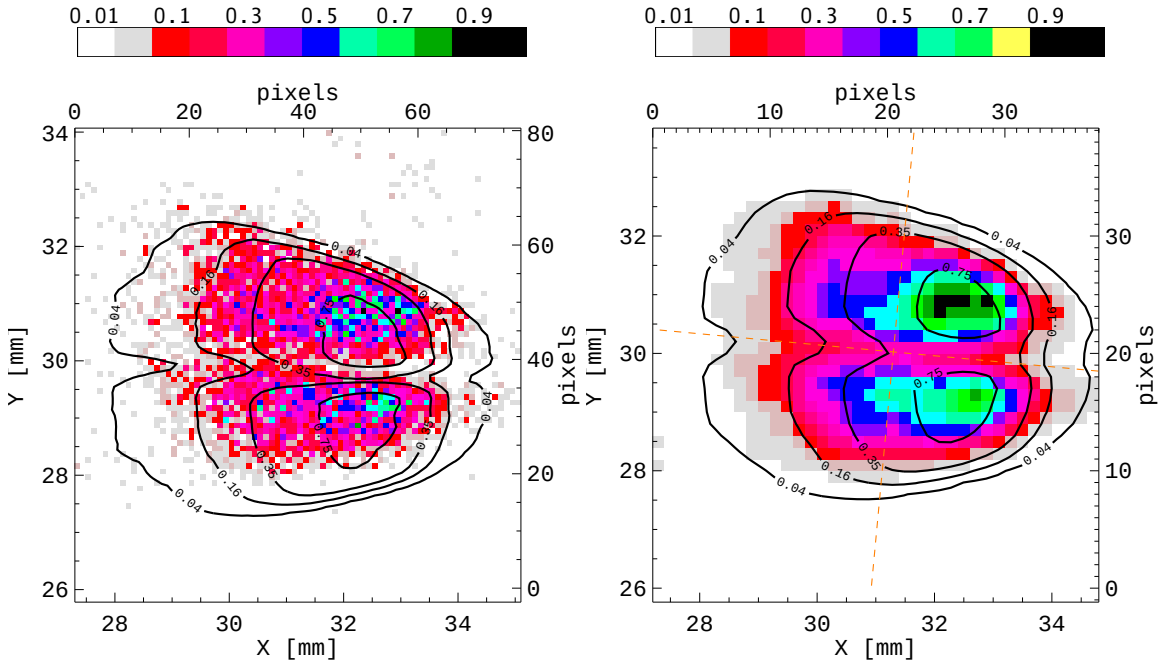

Figure 14. *Left*: Ray-tracing simulation of the COOL-X x-ray finger configuration at CAST. The source is located 14.2 m from the optic with a 6 mm diameter extension, and the simulation has a spatial resolution of 200 µm per pixel. *Right*: Measured scatter plot of the COOL-X x-ray source acquired at CAST with the Micromegas detector (375 µm spatial resolution) during the COOL-X run. The measurement corresponds to a total exposure time of just over 5 hours. The red dashed lines mark the XY center of the focal spot, that is calculated as the barycenter of all events registered during the COOL-X x-ray finger run. *Both panels:* black contours indicate intensity levels of 4%, 16%, 35% and 75% of the peak value.

2026 JINST 21 P03023

Table 4. Comparison of HPD for point like sources and the solar disk.

	50% HPD		80%		90%	
	[arcsec]	[mm]	[arcsec]	[mm]	[arcsec]	[mm]
Perfect Point Source	169	1.23	271	1.97	314	2.28
Point Source (fig. err.)	208	1.51	391	2.84	572	4.16
Perfect Solar Disk	196	1.42	306	2.22	363	2.64
Solar Disk (fig. err.)	234	1.70	422	3.07	589	4.28

Figure 15 (left), presents the actual Primakoff axion flux within the CAST coldbore (21.4 mm radius) in units of $\mathrm{keV}^{-1}\mathrm{s}^{-1}$ and compare it to the actual throughput from the Pathfinder x-ray optics. We obtain a total throughput efficiency of 29.78 ± 1.49%, where the uncertainty is mainly dominated by the systematic introduced by from the 8.0 Å PMMA layer discussed in section 4.2.2.

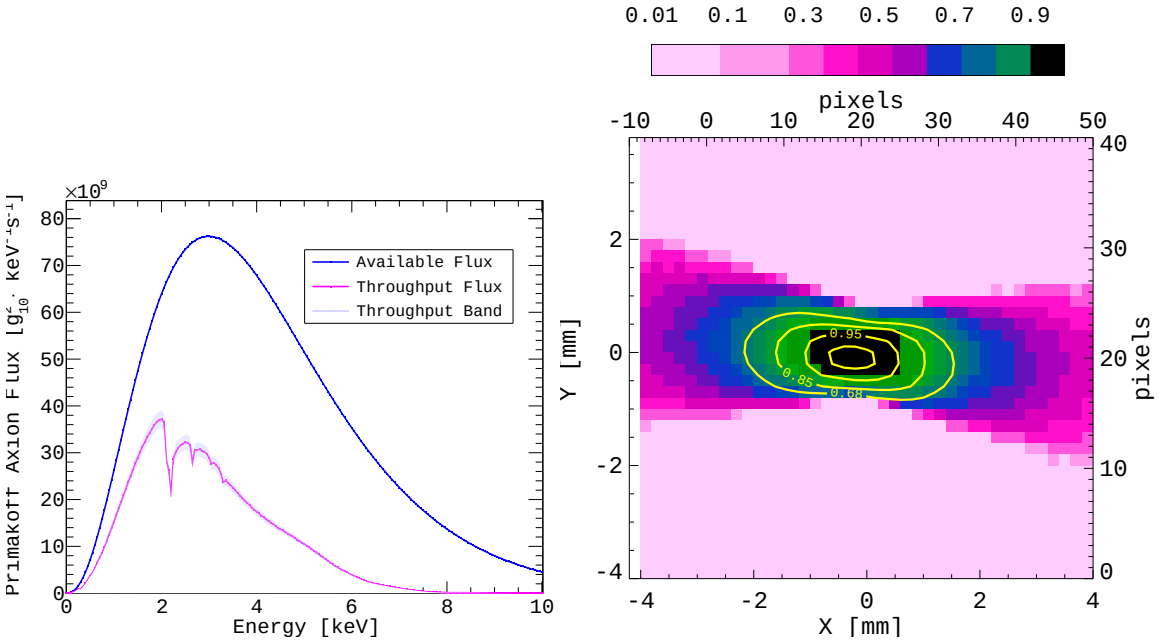

Figure 15. *Left*: expected Primakoff axion flux within the CAST coldbore (blue line) and actual throughput of the Pathfinder x-ray optics (magenta line). *Right*: ray-trace simulations of Primakoff signal (PSF) including spatial resolution of CAST's detector; closed contours (yellow) indicate the 99%, 95%, 85% and 68% signal-encircling regions.

The overall performance of the pathfinder telescope at CAST can be quantified through the signal-to-noise ratio enhancement, denoted as SN_{boost}. The sensitivity of an experimental setup such as ours to axion-photon couplings ($g_{a\gamma}$) depends not only on the number of signal photons reaching the detector, N_γ (i.e. the system throughput), but also on the background counts measured within the signal region, N_b. In the regime where the measurement is dominated by background events ($N_b > N_\gamma$), the discovery potential scales approximately as $N_\gamma/\sqrt{N_b}$. Since N_b is directly proportional to the area over which the signal is recorded, the sensitivity gain in axion-photon coupling

2026 JINST 21 P03023

achieved by the Pathfinder telescope can be expressed as

$$\mathrm{SN}_{\mathrm{boost}} = \frac{\epsilon_t}{\sqrt{s/A}}, \tag{5.1}$$

where ϵ_t is the total telescope efficiency, s is the effective spot size of the focused signal, and A is the total area of the magnet bore. Assuming that the x-ray detector exhibits equivalent background performance with and without the telescope, N_b can be considered identical in both cases.

Substituting the measured performance parameters of the Pathfinder during CAST data-taking periods yields a signal-to-noise enhancement factor of approximately 4. This result is obtained using the Pathfinder's spot size of 8 mm^2 and the CAST magnet bore area of 1438 mm^2 and it is derived from a combination of experimental characterization performed at the PANTER x-ray test facility and detailed ray-tracing simulations that provide the spatial and spectral distribution of the signal on the detector plane (see right panel of figure 15). Although the signal probability density function (PDF) exhibits some energy dependence, the majority of the flux is consistently concentrated within an area of only a few mm^2. Our ray-tracing simulations assume a solar axion flux originating from an extended source corresponding to the solar core, located effectively at infinity.

6 Conclusions

We have designed, built, and characterized a Pathfinder x-ray optic intended for the International Axion Observatory (IAXO). The Pathfinder represents the first scale prototype of the IAXO x-ray optics system and has been experimentally characterized at the PANTER x-ray test facility of the Max Planck Institute for Extraterrestrial Physics. Following its successful integration and operation at CAST, the Pathfinder provided a factor four enhancement in signal-to-noise ratio, thereby improving the overall experimental sensitivity to axion-photon couplings. These results demonstrate the feasibility and performance potential of the IAXO optic concept, validating both the optical design and the associated alignment and calibration procedures. The experience gained with the Pathfinder will directly inform the design and optimization of the next-generation optics to be implemented in IAXO. The use of the Pathfinder at CAST has allowed to reach unprecedented sensitivity levels in a helioscope, particularly in the axion-photon parameter space [7, 8] and in the axion-electron coupling exploration [14].

Acknowledgments

We gratefully acknowledge support from the U.S. National Science Foundation (NSF) under Award No. 0239812, the National Aeronautics and Space Administration (NASA) under Grant No. NAG5-10842, and the German Federal Ministry of Education and Research (BMBF) under Grant Nos. 05 CC2EEA/9 and 05 CC1RD1/0. Additional support was provided by the German Research Foundation (DFG) under Grant Nos. HO 1400/7-1 and EXC-153. Part of this work was carried out under the auspices of the U.S. Department of Energy by Lawrence Livermore National Laboratory under Contract No. DE-AC52-07NA27344. We also thank the CAST Collaboration for hosting the IAXO pathfinder optic and for their technical assistance in aligning and monitoring the pathfinder setup.

References

[1] R.D. Peccei and H.R. Quinn, *CP Conservation in the Presence of Instantons*, *Phys. Rev. Lett.* **38** (1977) 1440.

2026 JINST 21 P03023

[2] R.D. Peccei and H.R. Quinn, *Constraints Imposed by CP Conservation in the Presence of Instantons*, *Phys. Rev. D* **16** (1977) 1791.

[3] D.F.J. Kimball and K. van Bibber, *The Search for Ultralight Bosonic Dark Matter*, Springer (2023) [DOI:10.1007/978-3-030-95852-7].

[4] A.B. Aleksandrov et al., *Search for weakly interacting massive dark matter particles: state of the art and prospects*, *Usp. Fiz. Nauk* **191** (2021) 905.

[5] P. Sikivie, *Dark matter axions*, *Int. J. Mod. Phys. A* **25** (2010) 554 [arXiv:0909.0949].

[6] IAXO collaboration, *Future axion searches with the International Axion Observatory (IAXO)*, *J. Phys. Conf. Ser.* **460** (2013) 012002.

[7] CAST collaboration, *New CAST Limit on the Axion-Photon Interaction*, *Nature Phys.* **13** (2017) 584 [arXiv:1705.02290].

[8] CAST collaboration, *New Upper Limit on the Axion-Photon Coupling with an Extended CAST Run with a Xe-Based Micromegas Detector*, *Phys. Rev. Lett.* **133** (2024) 221005 [arXiv:2406.16840].

[9] IAXO collaboration, *Conceptual Design of the International Axion Observatory (IAXO)*, 2014 *JINST* **9** T05002 [arXiv:1401.3233].

[10] IAXO collaboration, *Conceptual design of BabyIAXO, the intermediate stage towards the International Axion Observatory*, *JHEP* **05** (2021) 137 [arXiv:2010.12076].

[11] CAST collaboration, *Search for 14.4-keV solar axions emitted in the M1-transition of Fe-57 nuclei with CAST*, *JCAP* **12** (2009) 002 [arXiv:0906.4488].

[12] L. Di Luzio et al., *Probing the axion-nucleon coupling with the next generation of axion helioscopes*, *Eur. Phys. J. C* **82** (2022) 120 [arXiv:2111.06407].

[13] F. Aznar et al., *A Micromegas-based low-background x-ray detector coupled to a slumped-glass telescope for axion research*, *JCAP* **12** (2015) 008 [arXiv:1509.06190].

[14] CAST collaboration, *Search for solar axions produced through the axion-electron coupling g_{ae} using a new GridPix detector at CAST*, *JHEP* **12** (2025) 009 [arXiv:2505.05909].

[15] M. Kuster et al., *The X-ray Telescope of CAST*, *New J. Phys.* **9** (2007) 169 [physics/0702188].

[16] H. Wolter, *Spiegelsysteme streifenden Einfalls als abbildende Optiken für Röntgenstrahlen*, *Annalen Phys.* **445** (1952) 94.

[17] M.J. Pivovaroff and T. Okajima, *Geometries for Grazing Incidence Mirrors*, in *Handbook of X-ray and Gamma-ray Astrophysics*, C. Bambi and A. Santangelo, eds., Springer Nature Singapore (2023), p. 1–21 [DOI:10.1007/978-981-16-4544-0_2-1].

[18] R. Petre and P.J. Serlemitsos, *Conical imaging mirrors for high-speed x-ray telescopes*, *Appl. Opt.* **24** (1985) 1833.

[19] CAST collaboration, *An improved limit on the axion-photon coupling from the CAST experiment*, *JCAP* **04** (2007) 010 [hep-ex/0702006].

[20] A.C. Jakobsen, *X-ray optics in new instruments for astro- and astroparticle physics*, Ph.D. Thesis, Technical University of Denmark, ongens Lyngby, Denmark (2015), https://findit.dtu.dk/en/catalog/56e83f9ad5d2b57e56000068.

[21] K.K. Madsen et al., *Optimizations of Pt/SiC and W/Si multilayers for the Nuclear Spectroscopic Telescope Array*, in the proceedings of the *Optics for EUV, X-Ray, and Gamma-Ray Astronomy IV*, San Diego, CA, U.S.A., August 4–6 (2009) [DOI:10.1117/12.826669].

2026 JINST 21 P03023

[22] T. Pardini et al., *Optical and multilayer design for the first Kirkpatrick-Baez optics for x-ray diagnostic at NIF*, in the proceedings of the *Target Diagnostics Physics and Engineering for Inertial Confinement Fusion II*, San Diego, CA, U.S.A., August 27–28 (2013) [DOI:10.1117/12.2024133].

[23] J. Ruz et al., *Direct measurement of 235U in spent fuel rods with Gamma-ray mirrors*, *Nucl. Instrum. Meth. A* **777** (2015) 15.

[24] M.J. Pivovaroff et al., *Progress of focusing x-ray and gamma-ray optics for small animal imaging*, in the proceedings of the *Penetrating Radiation Systems and Applications VII*, San Diego, CA, U.S.A., July 30–August 4 (2005) [DOI:10.1117/12.625925].

[25] M. Fernández-Perea et al., *Physics of Reflective Optics for the Soft Gamma-Ray Photon Energy Range*, *Phys. Rev. Lett.* **111** (2013) 027404.

[26] K.D. Joensen et al., *Design of grazing-incidence multilayer supermirrors for hard-x-ray reflectors*, *Appl. Opt.* **34** (1995) 7935.

[27] D.G. Stearns, *The scattering of x rays from nonideal multilayer structures*, *J. Appl. Phys.* **65** (1989) 491.

[28] NuSTAR collaboration, *The Nuclear Spectroscopic Telescope Array (NuSTAR) High-Energy X-Ray Mission*, *Astrophys. J.* **770** (2013) 103 [arXiv:1301.7307].

[29] P.N. Rao et al., *Investigation of long term stability of W/B4C multilayer structures*, *Thin Solid Films* **755** (2022) 139327.

[30] D.L. Windt, *IMD — Software for modeling the optical properties of multilayer films*, *Comput. Phys.* **12** (1998) 360.

[31] D.L. Windt, *Reduction of stress and roughness by reactive sputtering in W/B4C multilayer films*, in the proceedings of the *Optics for EUV, X-Ray, and Gamma-Ray Astronomy III*, San Diego, CA, U.S.A., August 29–30 (2007) [DOI:10.1117/12.730647].

[32] J.E. Koglin et al., *NuSTAR hard x-ray optics design and performance*, in the proceedings of the *Optics for EUV, X-Ray, and Gamma-Ray Astronomy IV*, San Diego, CA, U.S.A., August 4–6 (2009) [DOI:10.1117/12.826724].

[33] Data analyses were performed using ENVI® V.6.1. ENVI® is a registered trademark of NV5 Global, Inc.

[34] D. Spiga et al., *Re-testing the JET-X Flight Module No. 2 at the PANTER facility*, *Exper. Astron.* **37** (2013) 37.

2026 JINST 21 P03023